

HOW DEAD ARE DEAD GALAXIES? MID-INFRARED FLUXES OF QUIESCENT GALAXIES AT REDSHIFT $0.3 < Z < 2.5$: IMPLICATIONS FOR STAR FORMATION RATES AND DUST HEATING.

MATTIA FUMAGALLI¹, IVO LABBÉ¹, SHANNON G. PATEL¹, MARIJN FRANX¹, PIETER VAN DOKKUM², GABRIEL BRAMMER³, ELISABETE DA CUNHA⁴, NATASCHA M. FÖRSTER SCHREIBER⁵, MARISKA KRIEK⁶, RYAN QUADRI⁷, HANS-WALTER RIX⁴, DAVID WAKE⁸, KATHERINE E. WHITAKER⁹, BRITT LUNDGREN⁸, DANILO MARCHESINI¹⁰, MICHAEL MASEDA⁴, IVELINA MOMCHEVA², ERICA NELSON², CAMILLA PACIFICI¹¹, ROSALIND E. SKELTON¹²

Submitted to ApJ

ABSTRACT

We investigate star formation rates of quiescent galaxies at high redshift ($0.3 < z < 2.5$) using 3D-HST WFC3 grism spectroscopy and Spitzer mid-infrared data. We select quiescent galaxies on the basis of the widely used UVJ color-color criteria. Spectral energy distribution fitting (rest frame optical and near-IR) indicates very low star formation rates for quiescent galaxies ($\text{sSFR} \sim 10^{-12} \text{yr}^{-1}$). However, SED fitting can miss star formation if it is hidden behind high dust obscuration and ionizing radiation is re-emitted in the mid-infrared. It is therefore fundamental to measure the dust-obscured SFRs with a mid-IR indicator. We stack the MIPS-24 μm images of quiescent objects in five redshift bins centered on $z = 0.5, 0.9, 1.2, 1.7, 2.2$ and perform aperture photometry. Including direct 24 μm detections, we find $\text{sSFR} \sim 10^{-11.9} \times (1+z)^4 \text{yr}^{-1}$. These values are higher than those indicated by SED fitting, but at each redshift they are 20-40 times lower than those of typical star forming galaxies. The true SFRs of quiescent galaxies might be even lower, as we show that the mid-IR fluxes can be due to processes unrelated to ongoing star formation, such as cirrus dust heated by old stellar populations and circumstellar dust. Our measurements show that star formation quenching is very efficient at every redshift. The measured SFR values are at $z > 1.5$ marginally consistent with the ones expected from gas recycling (assuming that mass loss from evolved stars refuels star formation) and well above that at lower redshifts.

Subject headings: galaxies: evolution galaxies: formation galaxies: high-redshift

1. INTRODUCTION

A bimodal distribution in galaxy properties (star formation rate, size, morphology) has been observed in the local Universe (e.g. Kauffmann et al. 2003). This bimodality is made of blue, predominantly late-type galaxies, whose emission is dominated by young stellar populations and experiencing significant level of star formation (SF), complemented by red, early-type (elliptical or S0) galaxies dominated by an old stellar population with little or absent star formation.

The bimodality has been observed all the way to $z \sim 2$

¹ Leiden Observatory, Leiden University, P.O. Box 9513, 2300 RA Leiden, Netherlands

² Department of Astronomy, Yale University, New Haven, CT 06511, USA

³ European Southern Observatory, Alonso de Crdova 3107, Casilla 19001, Vitacura, Santiago, Chile

⁴ Max Planck Institute for Astronomy (MPIA), Knigstuhl 17, 69117 Heidelberg, Germany

⁵ Max-Planck-Institut fr extraterrestrische Physik, Giessenbachstrasse, D-85748 Garching, Germany

⁶ Department of Astronomy, University of California, Berkeley, CA 94720, USA

⁷ Observatories of the Carnegie Institution of Washington, Pasadena, CA 91101, USA

⁸ Department of Astronomy, University of Wisconsin, Madison, WI 53706, USA

⁹ Astrophysics Science Division, Goddard Space Flight Center, Code 665, Greenbelt, MD 20771, USA

¹⁰ Department of Physics and Astronomy, Tufts University, Medford, MA 02155, USA

¹¹ Yonsei University Observatory, Yonsei University, Seoul 120-749, Republic of Korea

¹² South African Astronomical Observatory, Observatory Road, Cape Town, South Africa

(Labbé et al. 2005, Kriek et al. 2006, Ilbert et al. 2010, Brammer et al. 2011, Whitaker et al. 2013).

Specific star formation rates from SED fitting and equivalent widths from emission lines indicate for quiescent galaxies very low values ($\log_{10}\text{SFR} \cdot \text{yr} < -12$) even at high redshift (Ciambur et al. 2013, Kriek et al. 2006, Whitaker et al. 2013), suggesting that these galaxies are really dead.

These levels of star formation are much lower than expected. Even if the galaxy would have stopped accreting new gas from the intergalactic medium, some gas should always become available again for star formation due to gas recycled from evolved stages of stellar evolution (e.g. Leitner & Kravtsov, 2010). If the low levels of star formation are confirmed, it could have important implications for gas recycling and the effectiveness of quenching at high redshift. Alternatively, it is possible that amounts of star formation have been overlooked in previous studies because of heavy obscuration by dust.

To address this question, in this paper we determine the obscured SFRs of quiescent galaxies up to redshift $z \sim 2.5$ using their 24 μm emission. In Section 2, we discuss the data. In Section 3, we describe the selection of QGs, and compare their star formation rates from optical and near-IR SED fitting to the values expected from the recycling of gas from mass loss. We additionally evaluate how much obscured star formation might be hidden in our selection: this proves the need of looking at a mid-IR indicator for SFR. In Section 4, we stack 24 μm thumbnails of QGs in order to measure their obscured SFR. We evaluate possible contributions to the mid-IR fluxes of QGs in Section 5. We discuss

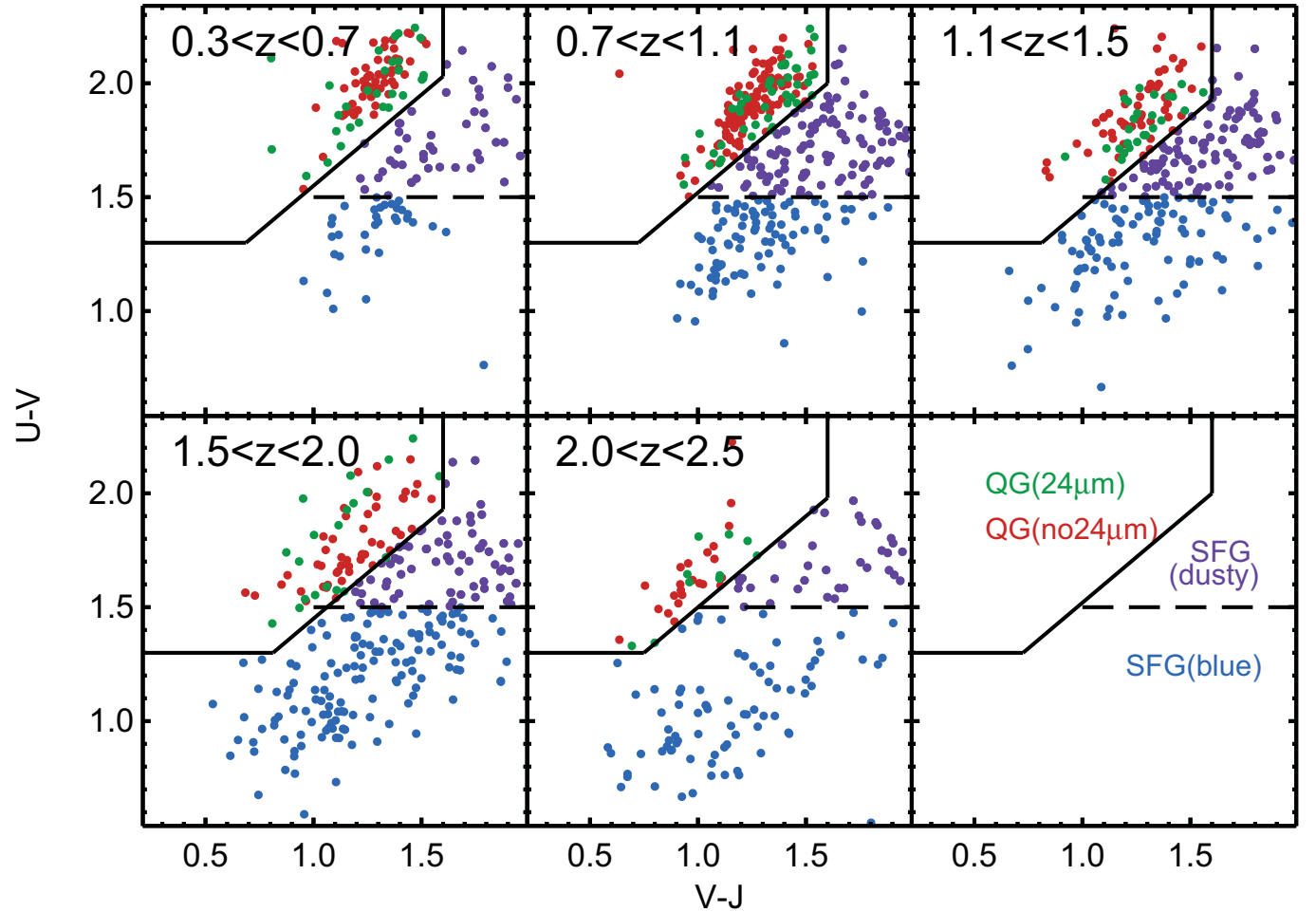


FIG. 1.— UVJ selection in different redshift bins, for mass selected samples ($\log(M/M_{\odot}) > 10.3$). The Whitaker et al. (2012) boundary divides (solid black line) quiescent and star forming galaxies. SFGs are subdivided into dusty ($U - V > 1.5$, purple dots) and unobscured ($U - V < 1.5$, blue dots). QGs are color coded according to the presence of a $24\mu\text{m}$ detection. We notice that $24\mu\text{m}$ detected galaxies do not preferentially lie in a particular locus of the UVJ diagram.

our findings in Section 6 and summarize them in Section 7. Through the paper we assume a standard cosmology with $H_0 = 70\text{ km s}^{-1}\text{ Mpc}^{-1}$, $\Omega_M = 0.30$, and $\Omega_\Lambda = 0.30$.

2. DATA

The 3D-HST Survey (van Dokkum et al. 2011; Brammer et al. 2012) is a 600 arcmin² survey using the Hubble Space Telescope (HST) to obtain complete, unbiased low-resolution near-IR spectra for thousands of galaxies. (Cycles 18 and 19, PI: van Dokkum).

It targets five fields (COSMOS, GOODS-S, GOODS-N¹³, AEGIS, UDS) where a wealth of ancillary multi-wavelength data is available (U band to $24\mu\text{m}$); they are crucial for interpreting spectra that often contain a single emission line, if any. The 3D-HST photometric catalogue is described in Skelton et al. (2013, in prep).

The WFC3 grism spectra have been extracted with a custom pipeline, described in Momcheva et al. (2013, in prep). Redshifts have been measured via the combined photometric and spectroscopic information using a

¹³ GOODS-N has been taken as part of program GO-11600 (PI: B. Weiner) and integrated into 3D-HST

modified version of the EAZY code (Brammer et al. 2008). The precision of redshifts is proven to be $\sigma(\frac{dz}{1+z}) = 0.3\%$ (Brammer et al. 2012, Momcheva et al. 2013).

Accurate redshifts allow the derivation of accurate rest-frame fluxes: we interpolate rest-frame filters from the observed SED with the Inter-rest code (Taylor et al., 2009), based on the algorithm by Rudnick et al (2003). Stellar masses have been determined using the FAST code by Kriek et al. (2009), using Bruzual & Charlot (2003) models, and assuming exponentially declining SFHs, solar metallicity and a Chabrier (2003) IMF.

In this paper we restrict the analysis to the GOODS-N and GOODS-S fields, for which very deep Spitzer-MIPS ($S_{24} = 10\mu\text{Jy}$, 3 σ) data are available (Dickinson et al., 2003), necessary for inferring low levels of SF. The MIPS $24\mu\text{m}$ beam has a FWHM of 6 arcsec, therefore confusion and blending effects are unavoidable in deep observations at this resolution. We perform photometry using a source-fitting algorithm (Labbé et al. 2006, Wuyts et al. 2007) that takes advantage of the higher resolution information contained in the F140W and F160W images.

Total IR luminosities ($L_{\text{IR}} = L(8 - 1000\mu\text{m})$) were de-

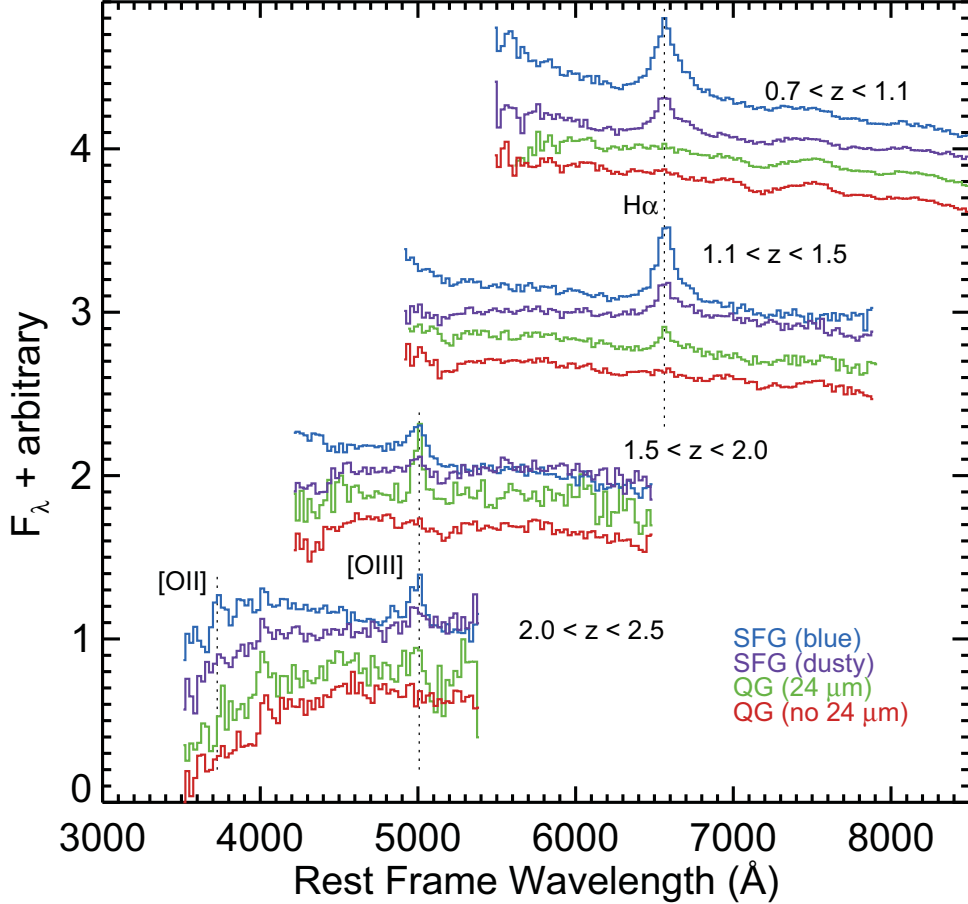


FIG. 2.— Stacked 3D-HST spectra for mass selected ($\log(M/M_\odot) > 10.3$) galaxies in different redshift bins. In each redshift bin, blue means blue SFGs ($U - V < 1.5$), purple dust reddened SFGs ($U - V > 1.5$), green QGs with a $24\mu\text{m}$ detection, red QGs without a $24\mu\text{m}$ detection. Vertical dashed lines show the position of $\text{H}\alpha$, $[\text{OIII}]$ and $[\text{OII}]$.

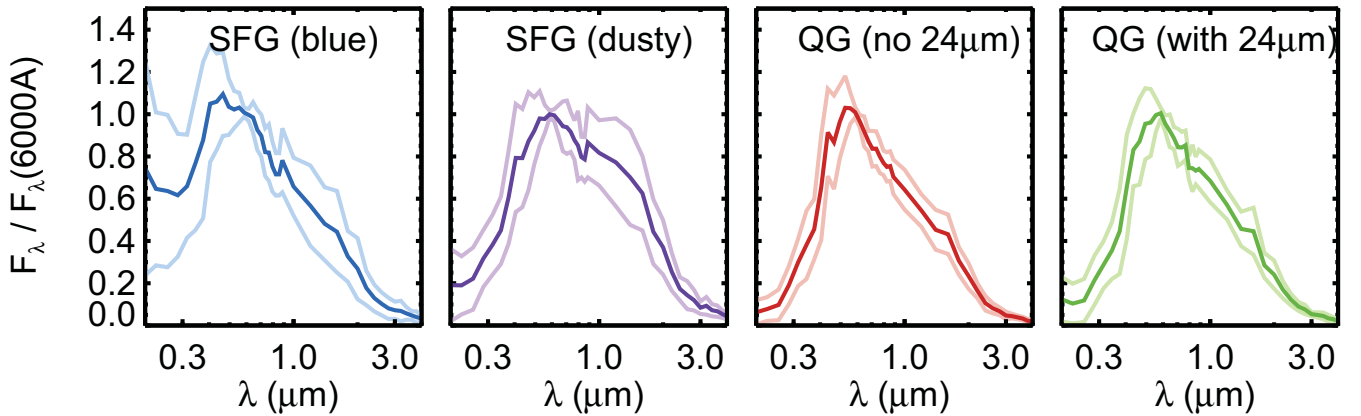


FIG. 3.— Composite SEDs for mass selected samples ($\log(M/M_\odot) > 10.3$) of star-forming galaxies (divided into blue and dusty) and quiescent galaxies (divided according to the presence of a $24\mu\text{m}$ detection) at redshift $0.3 < z < 2.5$. Light lines indicate the scatter in the stacks. Quiescent galaxies with and without $24\mu\text{m}$ detection have very similar optical and near-IR SEDs.

rived from the observed $24\mu\text{m}$ fluxes, on the basis of a single template that is the average of Dale & Helou (2002) templates with $1 < \alpha < 2.5$, following Wuyts et al. (2008) (see also Franx et al. 2008, Muzzin et al. 2010), and in good agreement with recent Herschel/PACS mea-

surements by Wuyts et al. (2011). SFRs are determined from the IR emission as in Kennicutt (1998) (adopted for a Chabrier IMF): $\text{SFR}(\text{IR}) = 0.98 \times 10^{-10} L_{\text{IR}}$. This quantity accounts properly just for obscured SF.

On the 3D-HST GOODS fields extremely deep X-ray

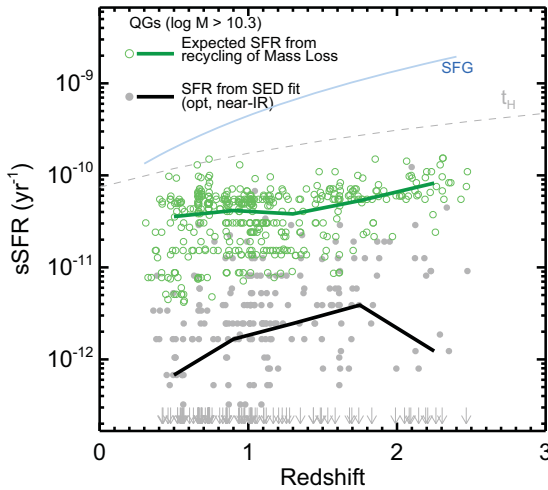


FIG. 4.— sSFR in different redshift bins (grey filled dots) and expected sSFR from recycling of gas from the mass loss of evolved stars (green open dots), as determined from FAST best fits to the SEDs of quiescent galaxies. Solid lines represent mean values in different redshift bins. The mass loss is computed from M_{gas} in BC03 models. It overpredicts the SFR by a factor of 20 at each redshift. SFRs of star forming galaxies on the main sequence (cyan) and the Hubble time (dashed grey) are shown as references.

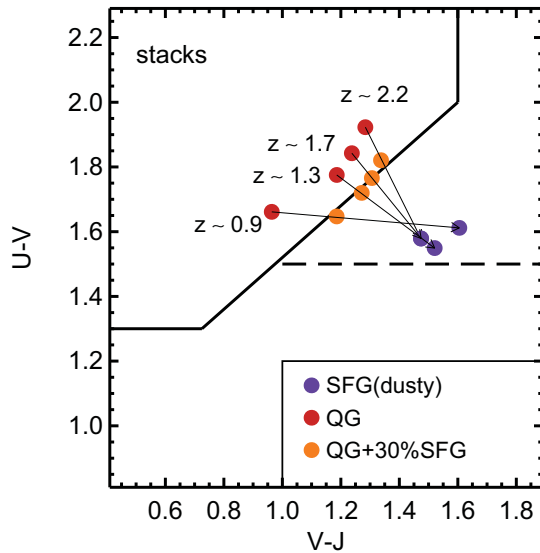


FIG. 5.— The UVJ position of stacks of QGs (red) and dusty SFGs (purple) at different redshifts is shown. Black arrows show the tracks obtained summing a variable fraction (normalized to 6000 \AA , F_{SFG}) of the dusty SFGs SEDs to the QGs SEDs. Orange dots show composite SEDs on the UVJ boundary, corresponding to $F_{\text{SFG}} = 30\%$.

data is also available, 4Ms in CDF-South (see Xue et al. 2011), and 2Ms in CDF-North (see Alexander et al. 2003), that we use for identifying bright AGNs.

3. SAMPLE SELECTION AND MOTIVATIONS OF THE STUDY

3.1. Selection of Quiescent Galaxies

In order to select quiescent galaxies (QGs) we use a color-color technique (Figure 1), specifically rest-frame

U-V versus rest-frame V-J (hereafter: UVJ diagram). This technique has been widely used to distinguish QGs from SFGs, including the heavily reddened SFGs (Labbé et al. 2005; Wuyts et al. 2007; Williams et al. 2009; Brammer et al. 2009; Whitaker et al. 2010; Patel et al. 2012; Bell et al. 2012; Gobat et al. 2013). QGs are identified using the criteria $(U - V) > 0.8 \times (V - J) + 0.7$, $U - V > 1.3$ and $V - J < 1.5$, as in Whitaker et al. (2012)¹⁴. Effectively, this selection targets galaxies whose optical and near-IR light is dominated by an old stellar population. We select galaxies more massive than $\log(M/M_{\odot}) > 10.3$ and divide the sample in five redshift bins, centered on $z = 0.5, 0.9, 1.2, 1.7, 2.2$. At each redshift the QG sample consists of at least 50 galaxies (Table 1).

3.2. Spectra and SEDs of the sample

In Figure 2 we show stacked optical spectra of QGs and SFGs from 3DHST in mass selected samples ($\log(M/M_{\odot}) > 10.3$). SFGs are subdivided into blue SFG ($U - V < 1.5$) and dust reddened SFGs ($U - V > 1.5$).

QGs are subdivided according to the presence of a MIPS $24\mu\text{m}$ detection. As noted by other authors (e.g. Brammer et al. 2009, Barro et al. 2013), approximately 25% of optically selected QGs have a $24\mu\text{m}$ detection, which is in apparent contrast with the red optical colors and the SEDs. We also notice that $24\mu\text{m}$ detected QGs do not lie preferentially in any locus of the UVJ diagram (green dots in Figure 1).

The spectra in Figure 2 clearly show that the UVJ selection is efficient in dividing the two populations; the SFG selection includes the heavy dust reddened SFGs, that despite red U-V colors, show spectral features ($\text{H}\alpha$, D4000) characteristic of SFGs. It is also noteworthy to see that QGs with $24\mu\text{m}$ detections have some $\text{H}\alpha$ and $[\text{OIII}]$ (cfr. Whitaker et al. 2013), that indicate the presence of low level star formation and/or nuclear activity.

Figure 3 shows composite SEDs (following the methodology of Kriek et al. 2011) for SFGs (divided into blue and dusty) and QGs (divided according to the presence of a $24\mu\text{m}$ detection). The SED shapes of star forming galaxies, dusty star forming galaxies and quiescent galaxies are clearly different. The rest-frame optical and near-IR SEDs of QGs with and without $24\mu\text{m}$ detection are instead very similar.

3.3. SFRs from SED fitting and expectations from gas recycling

We first analyze the specific star formation rates from the SED fits to the UV-optical and near-IR photometry (see Section 2). The values are shown against redshift for the quiescent galaxies in Figure 4 (grey dots and black line). The median value is $\text{sSFR} = 1.7 \times 10^{-12} \text{ yr}^{-1}$, and the correlation with redshift is weak. These values compare well with those of Ciambur et al (2013), who used a similar method. No significative difference in the SED derived SFRs is seen if we split the quiescent population between galaxies with and without a $24\mu\text{m}$ detection.

The low star formation rates can be compared to the stellar mass loss from evolved stellar populations (Par-

¹⁴ We test the stability of the selection by shifting the box by ± 0.05 magnitude, which does not affect the analysis.

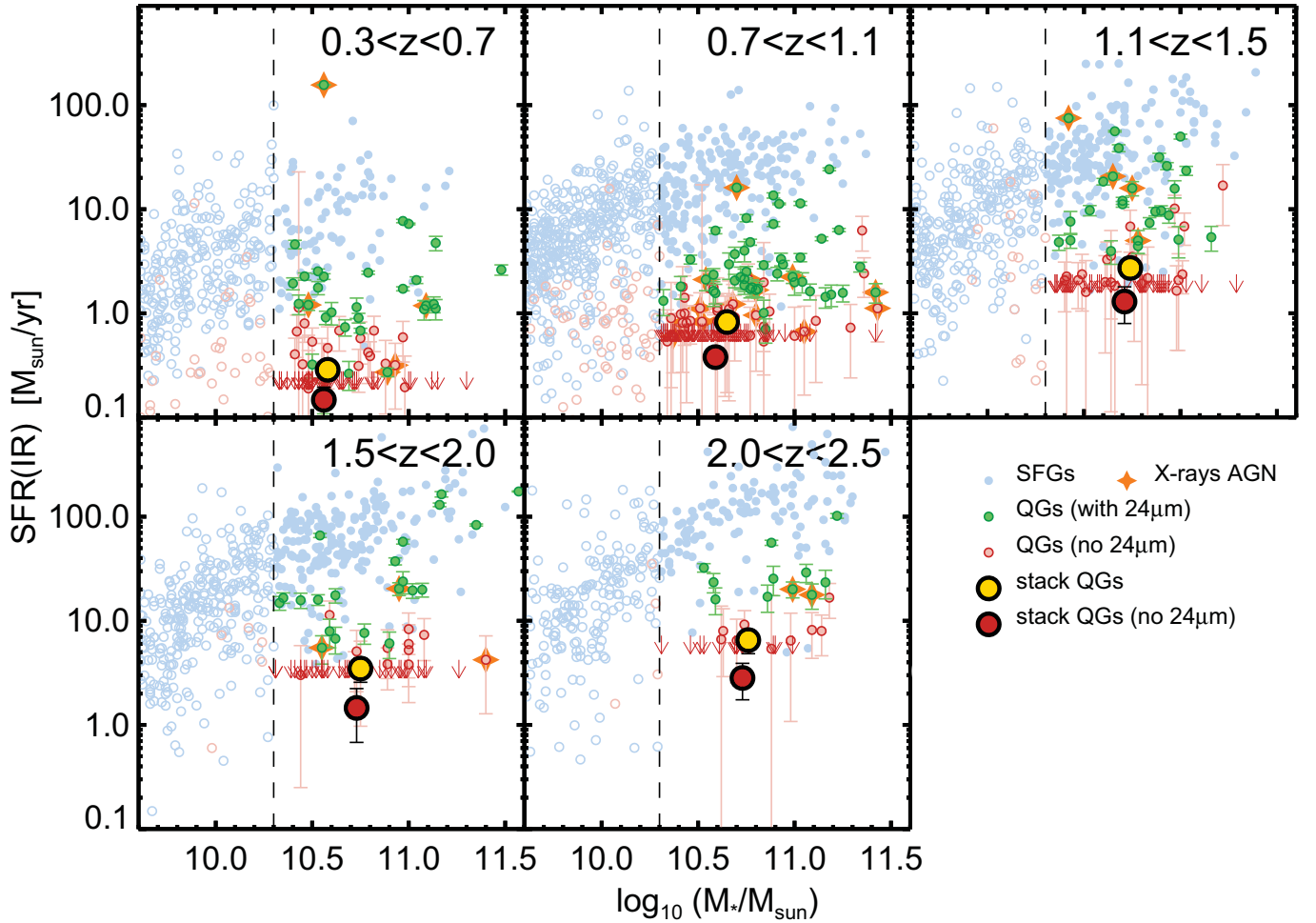


FIG. 6.— Mass-SFR(IR) diagram for galaxies in the 5 redshift bins analyzed in the paper. SFR are computed assuming that all of the 24μm flux is due to reprocessed UV photons from HII regions. Filled symbols denote galaxies with $\log(M/M_{\odot}) > 10.3$. Galaxies are divided in quiescent (QGs) and star-forming (SFGs) according to the box defined in Whitaker et al. (2012): light blue dots represent SFGs, green dots QGs detected in 24μm ($S/N > 3$), red dots QGs not detected in 24μm. Sources with $S/N < 1$ are shown as arrows at the 1σ level. Orange stars represent X-ray detected QGs in the CDF-S 4Ms catalog and CDF-N 2Ms catalog. The large red dots show the SFR obtained stacking thumbnails of individually undetected QGs (red), and all QGs (yellow), in mass selected samples of $\log(M/M_{\odot}) > 10.3$. Errors on the stacks are computed through bootstrapping of the sample.

riotti & Bregmann, 2008; Leitner & Kravtsov, 2010). Green dots in Figure 4 represent for the QG sample the sSFR expected from stellar mass loss, assuming that 100% of the gas expelled from old stars is recycled into star formation. Mass loss is computed directly from M_{gas} of the BC03 models at the best fit age of the galaxy, given the best fit τ model. The expected ssSFR from gas recycling is $2 - 4 \times 10^{-11} \text{ yr}^{-1}$, with a weak redshift dependence. It overpredicts the ssSFR from optical and near-IR SED fitting of more than one order of magnitude.

The discrepancy between the two values at each redshift tells us that one of the following options must hold true:

- a mechanism able to prevent the cooling of gas expelled from old stars and therefore the fueling of new SF exists, or
- SFRs from optical and near-IR best fitting are underestimated (and a lot of star formation shows up in the mid-IR).

In the rest of the paper we test the latter possibility measuring SFRs in the mid-IR, in order to prove the former.

3.4. How much star formation could be hidden?

We evaluate how much SF a galaxy can hide (with high dust obscuration), while still retaining red optical-NIR colors. We stack the rest frame SEDs of QGs and dusty SFGs in different redshift bins; to each QG SED we add a variable fraction (normalized in light at 6000Å, F_{SFG}) of the dusty SFG SED. Figure 5 shows the position in the UVJ diagram of the QGs stacks (red), the dusty SFGs stacks (purple) and the SED with $F_{\text{SFG}} = 30\%$ (orange), on the UVJ separation border. Adding a 30% dusty SFG SED to our typical QG SED would keep such a galaxy as quiescent under our selection criteria despite the non-negligible contribution of obscured star formation. Since the SFR of the average SFG evolves with redshift, $F_{\text{SFG}} = 30\%$ corresponds to $\text{sSFR} \sim 8 \times 10^{-11} \text{ yr}^{-1}$ at $z = 0.5$ and $\text{sSFR} \sim 3 \times 10^{-10} \text{ yr}^{-1}$ at $z = 2.2$. This

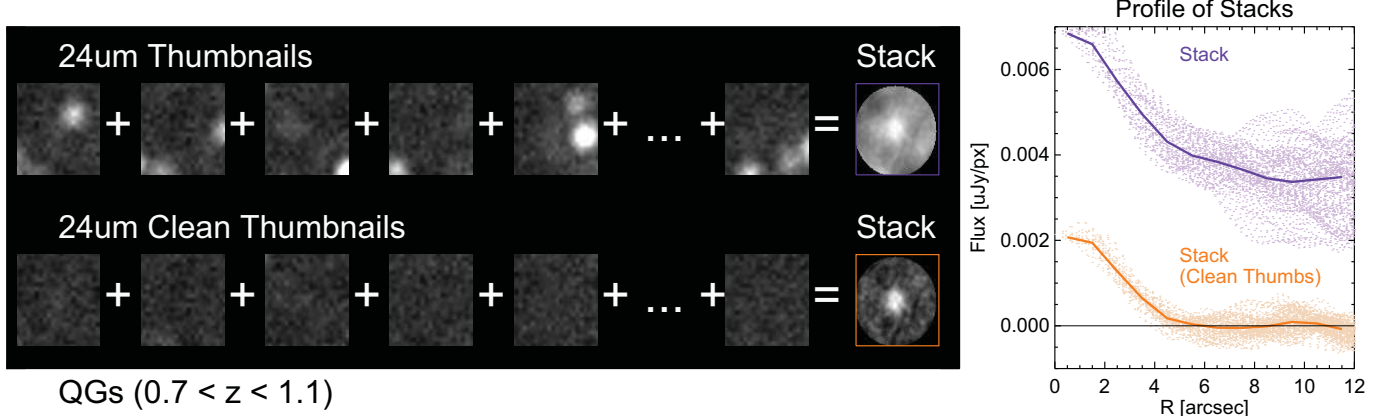


FIG. 7.— Stacking procedure for quiescent galaxies. Left: we show on the top row a random sample of $24\mu\text{m}$ postage stamps ($20''$ wide) from the QGs sample at $0.7 < z < 1.1$ and the resulting stack. The same postage stamps after the neighboring sources have been subtracted (with the PSF matching technique described in Section 2) are shown in the bottom row, along with the resulting mean stack. Right: Profile of the mean stacks (lines) and individual pixel values (dots) at their distance from the center. The 'normal' stack has a high, poorly constrained, background level (artificially raised by neighboring sources).

shows that with high dust content, a red (optical and near-IR) galaxy can hide a significant amount of SF. It is therefore necessary to measure SFR from MIR indicators in order to evaluate the SFRs of QGs. There is also a potential for entirely obscured populations with $A_V \gg 5$, which are known to exist the the centres of local dusty starbursting galaxies (e.g. Arp 220, Sturm et al. 1996).

4. MEASURING OBSCURED STAR FORMATION RATES OF QUIESCENT GALAXIES

In this Section we discuss the star formation rates determined from the IR emission with the methodology described in Section 2. In Figure 6 we plot the relation between stellar mass and SFR for galaxies in the mass-selected sample. As already noticed by various authors using a variety of SFR indicators (e.g. Noeske et al. 2007, Damen et al. 2009, Whitaker et al. 2012), SFRs and masses of SFGs are correlated (light blue dots), with a scatter of approximately 0.3 dex. The vast majority of the QGs lies in this plane below the 'star forming main sequence'. Most of the QGs are undetected in the MIPS $24\mu\text{m}$ at 3σ (red dots), while some of them (approximately 25 %, Table 1) have a $24\mu\text{m}$ detection (green dots), placing them in the Mass-SFR plane between SFGs and the detection limit.

In order to measure the SFRs for QGs, we stack $24\mu\text{m}$ thumbnails. We emphasize that in this step we stack *cleaned* images ($20''$ wide), where neighboring sources have been subtracted with the technique described in the Data section. Summing original $24\mu\text{m}$ thumbnails would lead to a stack with a very poorly constrained background, raised by the presence of neighboring objects. Since the goal of this paper is to measure very low SFRs with accuracy, it is fundamental to perform photometry on a stacked image with small uncertainty on the background (as shown in Figure 7).

We perform an average-stacking¹⁵ in different redshift bins, for two samples: all QGs and only non- $24\mu\text{m}$

detected QGs. Photometry on the stack is performed within a 3 arcsec aperture. Aperture fluxes are converted to total fluxes using a correction based on the MIPS $24\mu\text{m}$ PSF growth curve in the MIPS handbook ($F_{\text{tot}} = 2.5 \times F_{3''}$).

We obtain mostly clear detections with signal-to-noise of 3–5, and fluxes $F_{24\mu\text{m}} = 1 - 3\mu\text{Jy}$, corresponding to $\text{SFR} \sim 0.3\text{--}3 \text{ M}_\odot/\text{yr}$. We summarize the measured stacked fluxes in Table 1. Errors on the stacks are measured through bootstrapping of the sources. In Figure 6 we overplot with large yellow dots the SFR obtained from all QGs (big yellow dots) and non- $24\mu\text{m}$ detected galaxies (big red dots), representative of the deadest fraction of the galaxy population (this definition of 'quiescent galaxy' is the same as in Bell et al. 2012).

Despite the different sample selection (all QGs or just QGs non detected in $24\mu\text{m}$), it is evident that at each redshift the average QGs has a SFR which is at least $\sim 20 - 40$ times lower than the ones on the 'star forming sequence'.

In Figure 8 (left panel) we show the redshift evolution of SFRs of SFGs and QGs. We plot specific star formation rates ($\text{sSFR} = \text{SFR}/M_*$) since it is more mildly dependent on stellar mass than SFR itself. As noted by previous studies (e.g. Damen et al. 2010, Whitaker et al. 2012, Karim et al. 2012, Fumagalli et al. 2012), the evolution of sSFR in redshift for star forming galaxies is well fit by a power law $(1 + z)^n$ where $n \sim 3 - 4$. At each redshift QGs have a sSFR at least 20 times lower than SFGs. The evolution with redshift of sSFR of QGs seems to resemble the evolution of SFGs. At redshift $z \sim 2$, QGs form 10 times more stars than at redshift $z \sim 0.5$.

In Figure 9 we show for our samples the ratio of the average SFR of QGs to the average SFR of SFGs at the same redshift. For quiescent galaxies undetected in $24\mu\text{m}$, the mean value of the ratio is $\langle \text{SFR}_{\text{QG}} \rangle / \langle \text{SFR}_{\text{SFG}} \rangle = 1/(45 \pm 11)$ while for the entire sample it is $\langle \text{SFR}_{\text{QG}} \rangle / \langle \text{SFR}_{\text{SFG}} \rangle = 1/(22 \pm 7)$. This confirms that at each redshift quenching of star formation is very efficient.

¹⁵ Using instead median stacks does not modify the conclusions of the paper.

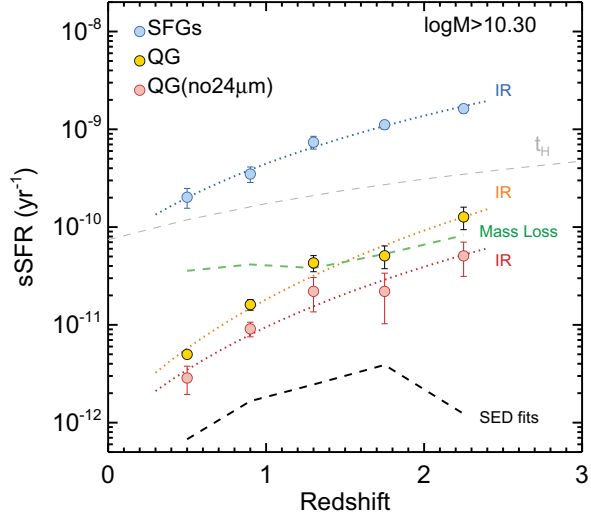


FIG. 8.— Left: Evolution of sSFR(IR) with redshift in a $\log(M/M_\odot) > 10.3$ mass selected sample. Light blue dots indicate mean values for SFGs, while yellow and red points are stacked values of non- $24\mu\text{m}$ detected QGs (red), and all QGs (yellow). At any redshift the average QG has a sSFR 20 times lower than the star-forming sequence. The evolution of sSFR of QGs resembles the one of SFGs. As in Figure 3, we indicate with a black line the sSFR from SED fitting and with a green line the expected SFR from mass loss. At high redshift SFR(IR) of QGs is comparable to the mass-loss. Right: Comparison of observed and modeled $L(\text{IR})/M_*$. Values from the stacks of quiescent are represented by dotted yellow and red lines. SFGs mean values (light blue) are put as a reference. Expected contributions to $L(\text{IR})$ for the QG samples from models described in Section 5 are drawn with solid lines (grey: AGN, orange: circumstellar dust, black: SFR from best fits, green: cirrus dust heating). Circumstellar dust and cirrus dust can account for most of the observed $L(\text{IR})$.

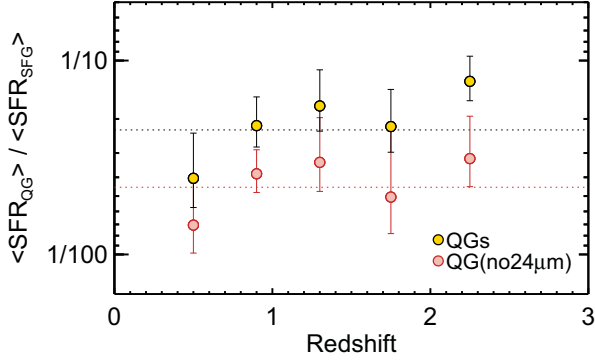
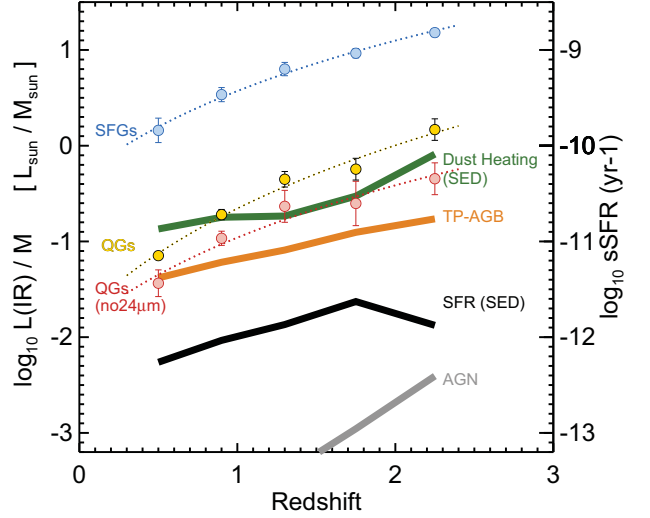


FIG. 9.— Ratio of the average SFR of QGs to the average SFR of SFGs at the same redshift. Red dots represent QGs which are individually undetected in $24\mu\text{m}$, while yellow dots represent all QGs. For the two samples, the average ratio is respectively $1/(45 \pm 11)$ and $1/(22 \pm 7)$. These ratios are possibly even lower because for QGs IR inferred SFRs can be significantly contaminated by other sources of dust heating (Section 5).

For QGs the SFRs inferred from the IR emission are generally an order of magnitude larger than those inferred from stellar population modeling (black dashed line in Figure 8, left panel). At the highest redshifts they are similar to the values predicted by the recycling of mass loss (green dashed line in Figure 8, left panel), while at redshift lower than 1.5 they are significantly lower than those.

5. OTHER POSSIBLE CONTRIBUTIONS TO $L(\text{IR})$

Strictly speaking, the IR-inferred SFRs for QGs are upper limits, because of contributions of AGNs, AGB stars and dust heating from old stellar populations to the IR fluxes. We treat each of these components separately in the following Subsections and compare their contribu-

tions to $L(\text{IR})$ with the observed stacked values of $L(\text{IR})$ in the Discussion Section.

5.1. AGN

We evaluate the possible contribution of AGNs by stacking X-rays thumbnails (from the CDF-S 4Ms and CDF-N 2Ms) of the QGs in different redshift bins. Mullaney et al. 2011 demonstrates (Equation 4) the existence of a linear relation between the X-ray luminosity $L(\text{Xray})$ and $L(\text{IR})$ for a sample of local AGNs. After subtracting individually detected X-ray point sources (marked with orange stars in Figure 6), we obtain marginal detections ($2 - 3\sigma$) ranging from $L_\text{X} \sim 3.8 \times 10^{40} \text{ erg/s}$ ¹⁶ in the lowest redshift bin to $L_\text{X} \sim 2.0 \times 10^{41} \text{ erg/s}$ in the highest redshift bin. Converting the obtained X-ray luminosities to IR luminosities with the Mullaney relation, we obtain the grey line in Figure 8 (right panel). It lies three orders of magnitude below the observed $L(\text{IR})/M_*$ ¹⁷. Olsen et al. (2012) suggest that at redshift $z \sim 2$ most QGs host a low-luminosity AGN, comparing SFR inferred from IR and X-rays. The two results are not in contradiction: even though AGNs can exist in those galaxies, they do not dominate the IR emission because of their low luminosity. Other studies (Donley et al. 2008; Kartaltepe et al. 2010) have already pointed out that systems with $24\mu\text{m}$ flux dominated by AGNs are not the dominant population at low $L(\text{IR})$.

5.2. Circumstellar dust

¹⁶ X-rays luminosities are evaluated assuming a power law spectrum with $\Gamma = 1.8$

¹⁷ A high fraction of Compton-thick AGNs in the sample would originate an higher IR luminosity inferred from X-ray stacks. The percentage of Compton-thick AGNs is however poorly constrained at high redshift (e.g. Akylas et al. 2012).

AGB stars are known to evolve embedded in a circumstellar dusty envelope (e.g. Bressan et al. 1998, Lançon & Mouhcine 2002, Piovan et al. 2003). They are the dominant source of the rest-frame K-band luminosity between 0.1 and 1.5 Gyr of age (Kelson & Holden 2010) and significantly contribute to MIR emission, but their dust contribution is not included in classical optical-near infrared SED fitting (Bruzual & Charlot 2003, Maraston 2005). We evaluate the contribution to $L(\text{IR})$ with the new Charlot & Bruzual 2010 model (CB2010) of an SSP with solar metallicity (private communication). Given galaxy ages from the FAST best fits (see Section 2, and Whitaker et al. 2013, in press), for each galaxy in our QG sample we estimate the observed $24\mu\text{m}$ flux from the CB2010 model and convert it to $L(\text{IR})$ with the same relation of Wuyts et al. (2008).

5.3. Cirrus dust

Another possible contribution to $L(\text{IR})$ is dust heating from old stellar populations. Salim et al. (2009) concludes that, for a sample of $24\mu\text{m}$ detected galaxies in the DEEP2 survey ($0.2 < z < 1.0$), the bulk of IR emission in red (NUV-r) galaxies comes from the heating of diffuse cirrus dust by old stellar populations, rather than by dust heating in star-forming regions. We test if this holds true for the galaxies in our sample as follows. Given the stellar population parameters from the FAST best-fit to the SEDs (age, τ , A_V), we evaluate the luminosity absorbed at $\lambda < 1\mu\text{m}$ integrating the difference between the unattenuated and the attenuated synthetic SED, and assume it is re-emitted in the IR (see Charlot & Fall 2000, Da Cunha et al. 2008).

We then compare the model $L(\text{IR})$ predicted by the attenuated SED with the best fit SFR. If $L(\text{IR})$ originates in dust associated with star-forming regions, we expect the ratio $L(\text{IR})/\text{SFR}$ to be $\sim 9.8 \times 10^9 L_\odot/M_\odot$ (Kennicutt, 1998). Figure 10 shows that SFGs (blue) are consistent with this prediction. On the other hand, for QGs (red points) $L(\text{IR})$ is systematically higher than the expectations from dust heating in star forming regions. This indicates that in QGs a significant contribution to $L(\text{IR})$ comes from dust heated by old stellar populations. Inferring SFR from $L(\text{IR})$ (and therefore from $24\mu\text{m}$ fluxes) overestimates the real SFR of QGs. For each galaxy in the QG sample we estimate the expected $L(\text{IR})$ luminosity from circumstellar dust, and compute the mean value in different redshift bins.

6. DISCUSSION

As we have seen above, various processes other than star formation can contribute to the observed mid-IR flux. We next discuss the impact on the derived SFRs. Moreover, we put constraints on the mass growth of QGs implied by the measured SFRs and on their size growth implied by the stellar mass loss.

In Figure 8 (right panel) we show the approximate evolution of L_{IR}/M_* , for data (dashed lines) and models (thick solid lines). We saw earlier that observations of $L(\text{IR})$ are based on the extrapolation of the single band $24\mu\text{m}$ to $L(\text{IR})$ assuming a template for dust heating by star forming regions (Section 2). Model predictions estimate that the AGN contribution (grey line) to the $L(\text{IR})$ is negligible for our sample, while the model expectation for $L(\text{IR})$ from cirrus dust (green) and circumstellar

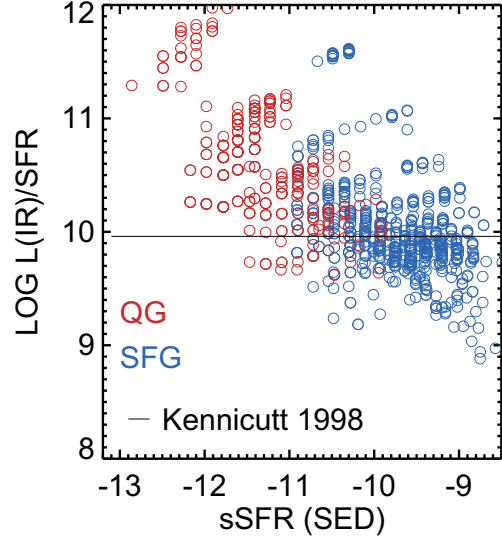


FIG. 10.— Model predictions of $L(\text{IR})/\text{SFR}$, for QGs (red) and SFGs (blue). $L(\text{IR})$ is reconstructed assuming that the light absorbed by dust at UV-optical wavelengths is re-emitted in the IR (Section 5). For SFGs the ratio is comparable to the Kennicutt (1998) relation (black line), while for QGs $L(\text{IR})$ are systematically higher than the expectations from SFR, meaning that for QGs most of dust heating comes from old stellar populations.

dust (orange) is comparable to the observed values from stacking. We note that qualitatively both of them decrease towards lower redshift, respectively because of the aging of galaxies (which leads to lower contribution of AGB stars in the SED) and because of higher A_V and lower ages at higher redshifts (which leads to more absorbed optical light re-emitted in the IR in the younger Universe).

If SFRs from SED fitting are correct, their contribution to $L(\text{IR})$ (black line in Figure 8, right panel) would be 1 dex lower than the observed $L(\text{IR})$, while dust heated by old stellar population can account for the most of the observed luminosities.

All the measured values from $24\mu\text{m}$ stacks must therefore be considered as upper limits to the SFR. At each redshift, the mean QG has a SFR at least $\sim 20\text{-}40$ times lower than that of a SFG at the same redshift. These values are significantly higher than estimates based on optical and near-IR model fits (see Section 3 and Ciambur, Kauffmann & Wuyts 2013).

Integrating the $\text{sSFR}(\text{IR})\text{-}z$ trend of Figure 8 (left), we estimate that the *maximum* growth of a QG via star formation is 20% from redshift 2 to 0. Some authors (e.g. van Dokkum et al. 2010, Patel et al. 2012) have estimated that a present day $10^{11.2} M_\odot$ galaxy has to grow 60% of its mass from redshift $z \sim 1.75$ to $z \sim 0$. We show that star formation can not be responsible for all the stellar growth of QGs, while other mechanisms must be in place, such as minor merging. The limit we compute on the mass increase via star formation is more stringent than that computed by Pérez-González et al. (2008), who estimates that massive spheroid-like galaxies may have doubled (at the most) their stellar mass from redshift 2 to 0.

The SFRs expected from stellar mass loss are probably

much higher than the real SFRs of QGs, meaning that star formation from mass loss is inefficient. If mass loss from evolved stars is not converted into stars and gas is expelled from the galaxy, an interesting consequence is that the potential of the system becomes shallower and the system expands (Zhao et al. 2002, Murray et al. 2010). In brief (following Damjanov et al., 2009), if a system loses a fraction $\delta M/M$ of its mass in a time longer than a dynamical timescale, it will expand its radius by a factor of $\delta R/R \sim (1 - \delta M/M)^{-1}$. The modeled mass losses for galaxies in our sample (Figure 4) integrated over the redshift range 0 to 2 give $\delta M/M \approx 0.4$, which leads to $\delta R/R \approx 0.6$. The observed size growth of quiescent galaxies from redshift 2 to 0 amounts to a factor of 2-3 (e.g. Williams et al. 2010, Newman et al. 2012, Whitaker et al. 2012), therefore mass loss can not be its unique cause but only one of the concurrent ones (see also Damjanov et al., 2009). We note that the assumed mass loss depends on the absolute ages of galaxies at each redshift, which are very uncertain.

7. CONCLUSIONS

We select quiescent galaxies at redshift $0.3 < z < 2.5$ in the 3D-HST survey from their rest-frame optical and near-IR colors. Fitting their UV to near-IR photometry with stellar population models, we find very low star formation rates ($sSFR \sim 10^{-12} \text{yr}^{-1}$). These values are much lower than the stellar mass loss rates predicted by the same models. This suggests that the star formation is either missed because it is dust obscured, or that the gas from stellar mass loss is expelled from the galaxy or prevented from refuelling star formation.

We put upper limits on the obscured star formation rate of quiescent galaxies by stacking $24\mu\text{m}$ images. Including direct $24\mu\text{m}$ detections, we find that $sSFR(\text{IR}) \leq 10^{-11.9} \times (1 + z)^4 \text{yr}^{-1}$. At each redshift the $sSFR$ of quiescent galaxies is $\sim 20\text{-}40$ times lower than the typical value on the main sequence of star forming galaxies. SFRs of quiescent galaxies are possibly even lower than this, because the IR luminosity can also be due to other sources, such as the presence of AGB dust enshrouded stars and dust heating from older stellar populations. Stacks of longer wavelength data (such as from Herschel) are necessary for constraining the dust temperature and therefore distinguishing between the different contributions to $L(\text{IR})$, however a large sample may be necessary to achieve adequate S/N (e.g. Viero et al. 2013). We show nevertheless that dust heating from old stellar populations can account for most of the observed $L(\text{IR})$.

The observed $SFR(\text{IR})$ are therefore upper limits to the real SFR, which are possibly one order of magnitude lower. This means that there must be a mechanism that not only shuts down star formation, but also keeps the galaxy dead for a long period of time, preventing the ejected gas from cooling and forming new stars. If gas from mass-loss is expelled from galaxies, we predict that it is responsible of a growth in stellar radii of 60% from redshift 2 to 0.

We acknowledge funding from ERC grant HIGHZ no. 227749. This work is based on observations taken by the 3D-HST Treasury Program (GO 12177 and 12328) with the NASA/ESA HST, which is operated by the Asso-

ciation of Universities for Research in Astronomy, Inc., under NASA contract NAS5-26555.

TABLE 1
PROPERTIES OF STACKS

Redshift	N _{QG}	F(24μm) _{QG}	SFR(IR) _{QG}	N _{QG,no24μm}	F(24μm) _{QG,no24μm}	SFR(IR) _{QG,no24μm}
0.3-0.7	97	2.83 ± 0.91μJy	0.14 ± 0.04M _⊙ /yr	67	5.66 ± 0.40μJy	0.28 ± 0.02M _⊙ /yr
0.7-1.1	154	3.04 ± 0.51μJy	0.37 ± 0.06M _⊙ /yr	108	4.89 ± 0.56μJy	0.85 ± 0.10M _⊙ /yr
1.1-1.5	84	3.27 ± 1.26μJy	1.29 ± 0.49M _⊙ /yr	58	6.90 ± 1.29μJy	2.72 ± 0.51M _⊙ /yr
1.5-2.0	72	2.20 ± 1.16μJy	1.45 ± 0.77M _⊙ /yr	51	5.01 ± 1.32μJy	3.40 ± 0.90M _⊙ /yr
2.0-2.5	35	2.33 ± 0.89μJy	2.82 ± 1.08M _⊙ /yr	25	5.29 ± 1.32μJy	6.52 ± 1.63M _⊙ /yr

For different redshift bins: number of galaxies in the quiescent sample (QG) and quiescent sample without 24μm detection (QG,no24μm), along with their stacked 24m fluxes, and the implied SFR from IR emission.

REFERENCES

Akylas, A., Georgakakis, A., Georgantopoulos, I., Brightman, M., & Nandra, K. 2012, *A&A*, 546, A98

Alexander, D. M., Bauer, F. E., Brandt, W. N., et al. 2003, *AJ*, 126, 539

Barro, G., Faber, S. M., Pérez-González, P. G., et al. 2013, *ApJ*, 765, 104

Bell, E. F., van der Wel, A., Papovich, C., et al. 2012, *ApJ*, 753, 167

Brammer, G. B., van Dokkum, P. G., & Coppi, P. 2008, *ApJ*, 686, 1503

Brammer, G. B., Whitaker, K. E., van Dokkum, P. G., et al. 2009, *ApJ*, 706, L173

Brammer, G. B., Whitaker, K. E., van Dokkum, P. G., et al. 2011, *ApJ*, 739, 24

Brammer, G., van Dokkum, P., Franx, M., et al. 2012, arXiv:1204.2829

Parriott, J. R., & Bregman, J. N. 2008, *ApJ*, 681, 1215

Bressan, A., Granato, G. L., & Silva, L. 1998, *A&A*, 332, 135

Bruzual, G., & Charlot, S. 2003, *MNRAS*, 344, 1000

Chabrier, G. 2003, *ApJ*, 586, L133

Charlot, S., & Fall, S. M. 2000, *ApJ*, 539, 718

Ciambur, B. C., Kauffmann, G., & Wuyts, S. 2013, *MNRAS*, 432, 2488

da Cunha, E., Charlot, S., & Elbaz, D. 2008, *MNRAS*, 388, 1595

Damen, M., Labbé, I., van Dokkum, P. G., et al. 2011, *ApJ*, 727, 1

Damjanov, I., McCarthy, P. J., Abraham, R. G., et al. 2009, *ApJ*, 695, 101

Dickinson, M., & GOODS Team 2004, *Bulletin of the American Astronomical Society*, 36, #163.01

Donley, J. L., Rieke, G. H., Pérez-González, P. G., & Barro, G. 2008, *ApJ*, 687, 111

Franx, M., van Dokkum, P. G., Schreiber, N. M. F., et al. 2008, *ApJ*, 688, 770

Fumagalli, M., Patel, S. G., Franx, M., et al. 2012, *ApJ*, 757, L22

Gobat, R., Strazzullo, V., Daddi, E., et al. 2013, arXiv:1305.3576

Ilbert, O., Salvato, M., Le Floc'h, E., et al. 2010, *ApJ*, 709, 644

Karim, A., Schinnerer, E., Martínez-Sansigre, A., et al. 2011, *ApJ*, 730, 61

Kartaltepe, J. S., Sanders, D. B., Le Floc'h, E., et al. 2010, *ApJ*, 709, 572

Kauffmann, G., Heckman, T. M., White, S. D. M., et al. 2003, *MNRAS*, 341, 54

Kelson, D. D., & Holden, B. P. 2010, *ApJ*, 713, L28

Kennicutt, R. C., Jr. 1998, *ApJ*, 498, 541

Kriek, M., van Dokkum, P. G., Franx, M., et al. 2006, *ApJ*, 649, L71

Kriek, M., van Dokkum, P. G., Labbé, I., et al. 2009, *ApJ*, 700, 221

Kriek, M., van Dokkum, P. G., Whitaker, K. E., et al. 2011, *ApJ*, 743, 168

Labbé, I., Huang, J., Franx, M., et al. 2005, *ApJ*, 624, L81

Labbé, I., Bouwens, R., Illingworth, G. D., & Franx, M. 2006, *ApJ*, 649, L67

Lançon, A., & Mouhcine, M. 2002, *A&A*, 393, 167

Leitner, S. N., & Kravtsov, A. V. 2011, *ApJ*, 734, 48

Maraston, C. 2005, *MNRAS*, 362, 799

Mullaney, J. R., Alexander, D. M., Goulding, A. D., & Hickox, R. C. 2011, *MNRAS*, 414, 1082

Muzzin, A., van Dokkum, P., Kriek, M., et al. 2010, *ApJ*, 725, 742

Murray, N., Quataert, E., & Thompson, T. A. 2010, *ApJ*, 709, 191

Newman, A. B., Ellis, R. S., Bundy, K., & Treu, T. 2012, *ApJ*, 746, 162

Noeske, K. G., Weiner, B. J., Faber, S. M., et al. 2007, *ApJ*, 660, L43

Olsen, K. P., Rasmussen, J., Toft, S., & Zirm, A. W. 2013, *ApJ*, 764, 4

Patel, S. G., Holden, B. P., Kelson, D. D., et al. 2012, *ApJ*, 748, L27

Pérez-González, P. G., Trujillo, I., Barro, G., et al. 2008, *ApJ*, 687, 50

Piovan, L., Tantalo, R., & Chiosi, C. 2003, *A&A*, 408, 559

Rudnick, G., Rix, H.-W., Franx, M., et al. 2003, *ApJ*, 599, 847

Salim, S., Dickinson, M., Michael Rich, R., et al. 2009, *ApJ*, 700, 161

Sturm, E., Lutz, D., Genzel, R., et al. 1996, *A&A*, 315, L133

Taylor, E. N., Franx, M., van Dokkum, P. G., et al. 2009, *ApJS*, 183, 295

van Dokkum, P. G., Whitaker, K. E., Brammer, G., et al. 2010, *ApJ*, 709, 1018

Viero, M. P., Moncelsi, L., Quadri, R. F., et al. 2013, arXiv:1304.0446

Xue, Y. Q., Luo, B., Brandt, W. N., et al. 2011, *ApJS*, 195, 10

Whitaker, K. E., van Dokkum, P. G., Brammer, G., et al. 2010, *ApJ*, 719, 1715

Whitaker, K. E., van Dokkum, P. G., Brammer, G., & Franx, M. 2012, *ApJ*, 754, L29

Whitaker, K. E., van Dokkum, P. G., Brammer, G., et al. 2013, *ApJ*, 770, L39

Williams, R. J., Quadri, R. F., Franx, M., van Dokkum, P., & Labbé, I. 2009, *ApJ*, 691, 1879

Wuyts, S., Labbé, I., Franx, M., et al. 2007, *ApJ*, 655, 51

Wuyts, S., Labbé, I., Schreiber, N. M. F., et al. 2008, *ApJ*, 682, 985

Wuyts, S., Förster Schreiber, N. M., Lutz, D., et al. 2011, *ApJ*, 738, 106